JOURNAL OF AIRCRAFT
Vol. 32, No. 4, July–August 1995

Unstructured Adaptive Mesh Computations of Rotorcraft High-Speed Impulsive Noise

Roger C. Strawn* and Rupak Biswas†
NASA Ames Research Center, Moffett Field, California 94035
and
Michael Garceau‡
Stanford University, Stanford, California 94305

A new method is developed for modeling helicopter high-speed impulsive (HSI) noise. The aerodynamics and acoustics near the rotor blade tip are computed by solving the Euler equations on an unstructured grid. A stationary Kirchhoff surface integral is then used to propagate these acoustic signals to the far field. The near-field Euler solver uses a solution-adaptive grid scheme to improve the resolution of the acoustic signal. Grid points are locally added and/or deleted from the mesh at each adaptive step. An important part of this procedure is the choice of an appropriate error indicator. The error indicator is computed from the flowfield solution and determines the regions for mesh coarsening and refinement. Computed results for HSI noise compare favorably with experimental data for three different hovering rotor cases.

Introduction

THE reduction of rotor noise is an important goal for both civilian and military helicopters. Among the many contributors to rotor noise, one of the loudest and most annoying is called high-speed impulsive (HSI) noise. Impulsive noise is characterized by a strong acoustic disturbance that occurs over a very short period of time.

The production of HSI noise is strongly affected by a phenomenon known as flowfield delocalization. Delocalization occurs when the rotor speed increases to a point where supersonic flow on the rotor surface connects to the supersonic region beyond the linear sonic cylinder. The sonic cylinder is defined as the surface on which the relative speed between the undisturbed freestream and an observer on the blade has a Mach number equal to 1. An example of delocalized flow is shown in Fig. 1. In this case, the flowfield is not delocalized when the hover tip Mach number M_t is less than 0.9. Delocalization occurs when M_t is increased beyond 0.9, and the acoustic signal shows a dramatic increase in strength.

Once the flow on the rotor has delocalized, the surface shock is free to propagate to the far field with little dissipation. The resulting impulsive signal is perceived as a loud periodic "popping" sound. The delocalization phenomena is highly dependent on nonlinear transonic effects that occur near the blade tip. For this reason, linear methods,[1] that are based on the Ffowcs Williams and Hawkings[2] equation, cannot accurately model this type of noise.

Numerical solutions of the full-potential, Euler, or Navier–Stokes equations provide better models for these transonic flow nonlinearities. Their main drawback, however, is that it is computationally expensive to accurately solve the equations over large domains. An excellent compromise is to model the near-field transonic flow with a nonlinear computational fluid dynamics (CFD) method, and to couple this near-field solution to a Kirchhoff integral formula. The Kirchhoff formulation[3] integrates a known pressure field over a prescribed surface, and then propagates this to the far field. This Kirchhoff integration is much more computationally efficient than its CFD counterpart.

Purcell and his colleagues[4–7] were the first to use CFD models to study the HSI noise problem. Their method solved the full-potential equation to model the blade-tip aerodynamics. The near-field CFD solution was then coupled to a nonlinear Kirchhoff integral formula to propagate the acoustic signal to the far field. A similar approach has been taken by Xue and Lyrintzis[8] using a rotating Kirchhoff formulation. In both cases, the computed results showed reasonably good agreement with experimental data for hovering rotors.

In other work, Baeder[9,10] has modeled the same HSI noise problem for rotors in both hover and forward flight with CFD solutions to the Euler equations. The use of grid clustering along the expected path of the acoustic signal enabled it to

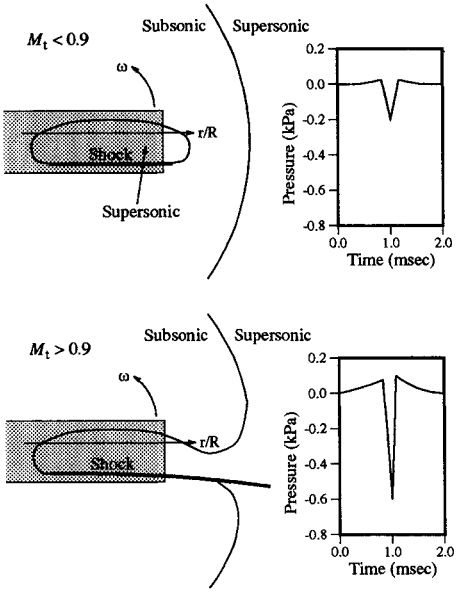

Fig. 1 Schematic of delocalization and helicopter rotor noise.

Presented as Paper 93-4359 at the AIAA 15th Aeroacoustics Conference, Long Beach, CA, Oct. 25–27, 1993; received Nov. 11, 1993; revision received Dec. 1, 1994; accepted for publication Dec. 30, 1994.

*Research Scientist, U.S. Army Aviation and Troop Command, Aeroflightdynamics Directorate, M/S 258-1. Member AIAA.
†Scientist, Research Institute for Advanced Computer Science, M/S T27A-1. Member AIAA.
‡Graduate Student, Department of Aerospace Engineering.

be accurately captured out to three rotor radii. The structured-grid Euler solver has also been coupled to a stationary Kirchhoff method that propagates the acoustic signal to the far field.[11]

A key feature of HSI noise signals is that they are confined to a very narrow region as they propagate away from the rotor blade. An accurate CFD simulation must concentrate grid points along the path of this acoustic signal in order to minimize numerical dissipation. All of the CFD approaches described earlier make use of structured grids to discretize the flowfield. It is very difficult to locally insert and delete points in a structured mesh. This makes it hard to dynamically increase the grid resolution along the HSI noise signals since their trajectories are generally not known in advance of the computation.

The alternative approach in this article is to use a solution-adaptive unstructured-grid solver to model the aerodynamic and acoustic fields close to the rotor blade. The major advantage of unstructured grids is the ability to efficiently insert and delete points in the computational mesh. Thus, the grid can locally adapt to improve the resolution of important flow features. The HSI noise problem is a good candidate for solution-adaptive schemes because the acoustic wave is very distinct in both the near and far fields. This makes it easy to identify the regions of the grid that need refinement.

This article demonstrates a new solution-adaptive CFD scheme for solving the aerodynamic and acoustic fields around hovering rotor blades. The near field is modeled with an unstructured-grid Euler solver, whereas the far-field acoustic propagation is computed using a newly developed Kirchhoff integral method. The combined approach forms a powerful tool for determining both near- and far-field HSI noise.

Euler Flow Solver

The near-field aerodynamics and acoustics are modeled with a modified version of the three-dimensional Euler solver developed by Barth.[12] The finite volume upwind scheme solves for solution variables at the vertices of the mesh and satisfies the integral conservation laws on nonoverlapping polyhedral control volumes surrounding these vertices. Improved accuracy is achieved by using a piecewise linear reconstruction of the solution in each control volume. This improved spatial accuracy hinges heavily on the calculation of the solution gradient in each control volume given pointwise values of the solution at the vertices of the mesh. The solution is advanced in time using conventional explicit procedures.

A rotary-wing version of this code was developed by Strawn and Barth.[13] The governing Euler equations have been rewritten in an inertial reference frame so that the rotor blade and grid system move through stationary air at the specified rotational and translational speeds. Fluxes across each computational control volume were computed using the relative velocities between the moving grid and the stationary far field.

An important highlight is that the code uses an edge-based data structure rather than one based on elements. Edges of a mesh are defined as the lines that connect pairs of vertices. Since the number of edges is significantly smaller than the number of faces, cell-vertex edge schemes are more efficient than cell-centered element methods.[12] Furthermore, an edge-based method does not limit the mesh to a particular volume element. Even though tetrahedral elements are used in this article, any arbitrary combination of polyhedra could be used.

Mesh Adaption Scheme

Two types of solution-adaptive mesh strategies have recently been used with unstructured-grid methods. The first is a grid regeneration scheme where an initial solution is obtained on a coarse mesh and then some error indicator is used to designate regions in the flowfield where additional grid points are required. The mesh is then regenerated with a higher concentration of points in these targeted flow regions. One major disadvantage of this scheme is that it is computationally intensive. This is a drawback for unsteady problems where the mesh must be frequently adapted. However, the resulting grids are usually well-formed with smooth transitions between regions of coarse and fine mesh spacing.

A second strategy for producing solution-adaptive meshes involves local modification of the existing grid in regions where the solution is either changing rapidly or remaining relatively constant. Grid points are individually added to the existing mesh in regions where an error indicator is high, and removed from regions where the indicator is low. The advantage of this strategy is that relatively few points need to be deleted or added at each coarsening/refinement step. However, complex logic and data structures are required to keep track of the points that are added and removed. Because of the importance of flowfield unsteadiness in rotorcraft problems, we have chosen this local grid modification scheme as the basis for our dynamic mesh adaption.

The three-dimensional mesh adaption scheme is described by Biswas and Strawn.[14] It requires an initial solution on a coarse tetrahedral mesh. An error estimate is then computed for every edge of the mesh and is used to determine the regions to be adapted. Particular attention is paid to the data structure so that a tetrahedral mesh can be rapidly recreated after grid points are removed and/or inserted. The points can be added or deleted in an anisotropic manner in order to efficiently resolve directional flow features. The goal is to optimally distribute the mesh points for a given error indicator.

Error Indicator for HSI Noise

Simple error estimates based on gradients of flowfield quantities have been used by several researchers. These types of error indicators are easy to implement and have simple physical interpretations. More complicated error indicators could be used, but they are probably not necessary for HSI acoustics problems. Generally, almost any reasonable error indicator can adequately target an impulsive signal such as an acoustic wave or a shock.

Since we are interested in computing acoustic pressure signals, we have chosen pressure differences across edges of the mesh to indicate flowfield regions that require mesh refinement or coarsening. This error indicator works well both on the blade surface and near the blade tip; however, it does not adequately target the far-field acoustic wave for refinement. This is because the strength of an HSI noise signal decreases rapidly as it goes farther away from the blade tip. In fact, the peak minimum acoustic pressure has been shown[5] to attenuate as

$$|P_{\min}(r) - P_\infty| \sim \frac{1}{\sqrt{(r/R_{sc})^2 - 1}}, \qquad r > R_{sc} \qquad (1)$$

where $P_{\min}(r)$ is the minimum local pressure at radial distance r from the hub, P_∞ is the freestream pressure, and R_{sc} is the radial location of the linear sonic cylinder.

This brings up an interesting general problem for error indicators. If the goal of the error indicator is simply to minimize the global error in the solution, then it should probably always target regions on the blade for refinement. This is because the pressure disturbances on the blade are much larger than those in the far field; hence, the error magnitude may also be greater there. This is true even though the far-field acoustic pressures may have a very large relative error. The objective in this article is to resolve the acoustic signal in both the near and far fields, not just to reduce the global error in the solution. Hence, error estimates for the far-field acoustic signals must be weighted equally with those on the blade surface.

Equation (1) can be used to help determine a proper weighting factor away from the blade tip. If the general shape of the HSI acoustic wave is assumed to remain constant, the

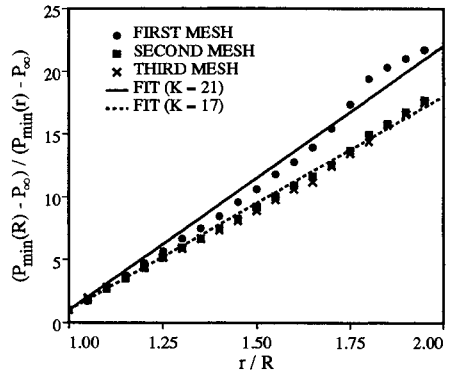

Fig. 2 Acoustic pressure curve fits for $M_t = 0.95$.

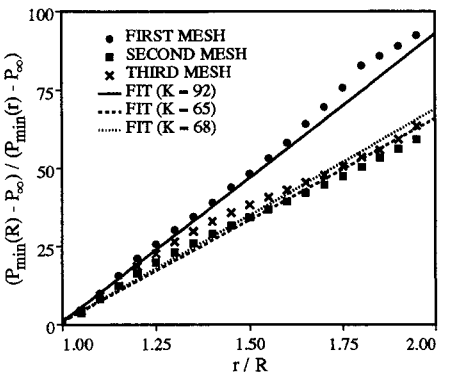

Fig. 3 Acoustic pressure curve fits for $M_t = 0.88$.

error indicator should scale by Eq. (1). However, Eq. (1) is undefined between the blade tip and the linear sonic cylinder. A better choice is a function that behaves asymptotically like Eq. (1), but is well-defined everywhere beyond the blade tip. Such a function is given by

$$\frac{|P_{min}(r) - P_\infty|}{|P_{min}(R) - P_\infty|} = \frac{1}{1 + K[(r/R) - 1]}, \qquad r \geq R \quad (2)$$

where R is the radial tip location and K is a constant that is determined from the computed solution on the mesh that is ready to be adapted.

Equation (2) is an excellent representation of the behavior of the acoustic wave for HSI noise. An example of this is shown in Fig. 2 where the computed pressure data for various meshes is compared with the curve fits obtained from Eq. (2). For this case, $M_t = 0.95$ and the acoustic flowfield is delocalized. Each of the three meshes in the figure has a different resolution in the region of the acoustic wave. These meshes will be described later in this article. It is remarkable that the curve-fits from Eq. (2) represent these minimum acoustic pressures so well, for both coarse and fine meshes. Similarly good results for the curve fits were obtained for the $M_t = 0.9$ test case that also shows a delocalized acoustic wave.

The final test case has $M_t = 0.88$ and is not delocalized. Curve-fits for this case are shown for three different mesh resolutions in Fig. 3. Note that these curve-fits do not match the minimum pressure data quite as well as for the two higher Mach number delocalized cases. The effects of this mismatch will be discussed in the next section.

Based on the curve-fits for HSI noise, we can write our scaled error indicator as

$$E_e = \begin{cases} |\Delta P| & \text{if } r \leq R \\ |\Delta P|\{1 + K[(r/R) - 1]\} & \text{if } r > R \end{cases} \quad (3)$$

where $|\Delta P|$ is the pressure difference across an edge and is nondimensionalized by freestream density and speed of sound squared. Note that there is no analytical expression for K, which is instead, determined by fitting the minimum pressure data on the mesh to be adapted.

Mesh Adaption Results

All three test cases chosen for this article are rectangular-blade rotors in hover with NACA 0012 cross sections and aspect ratios of 13.71. The calculations have $M_t = 0.95$, 0.90, and 0.88, respectively. The first two cases show significant delocalization at the tip, while the third is not delocalized. These conditions correspond to experimental cases tested by Purcell.[6,7] They have been successfully simulated by a number of researchers[4-11]; however, direct comparisons to these other efforts will be limited. The primary purpose of the calculations in this article is to demonstrate the capabilities of the new computational method.

The first task in the mesh adaption strategy is to choose an initial mesh. There are conflicting requirements for this mesh. First, it is desirable to simplify the mesh generation process as much as possible. A robust and generalized solution-adaptive procedure should be able to begin with an arbitrary initial mesh and eventually reach an adapted final mesh that has sufficient resolution to capture important flowfield features. However, a totally general mesh could result in an extremely coarse grid in the far field. The error indicators from the resulting solution may be so inaccurate that the presence of the propagating acoustic wave is completely missed. Clearly, an initial mesh requires some minimum far-field resolution in order to identify the presence of an acoustic signal.

The initial meshes chosen for these simulations are modified versions of the meshes used by Baeder.[10] These meshes have been chosen largely for convenience. Because the rotors are nonlifting, the mesh only needs to cover the upper half plane due to symmetry. The original structured grids had dimensions of 49 × 37 × 31 and extended out to three rotor radii in the spanwise direction. In order to obtain a coarser initial grid for the current calculations, every other point was used in both the chordwise and the normal directions to the rotor surface. This reduced the grid size by a factor of four. Also, the outer spanwise boundary for the calculation was reduced to two rotor radii.

Unstructured tetrahedral grids were created from these meshes by dividing each hexahedral element into five tetrahedra. The resulting unstructured grids contain 13,967 vertices, 60,986 tetrahedra, and 6818 triangular boundary faces. The outer boundaries of the mesh for the $M_t = 0.90$ case are shown in Fig. 4. Note that there is already some clustering along the expected path of the acoustic wave. The mesh adaption scheme will increase the resolution in this region.

An initial solution is computed on the coarse mesh by running 1000 iterations of the explicit flow solver. This required about 20 CPU minutes on a Cray C-90 computer. The converged solution is then used to compute an error indicator for the refinement step to follow. For $M_t = 0.95$, the error indicator is computed from Eq. (3) using $K = 21$. This value

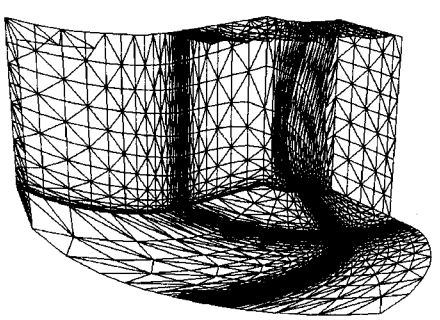

Fig. 4 Boundaries of the initial mesh for $M_t = 0.90$.

of K was determined from Fig. 2. Approximately 10,000 edges are targeted for subdivision and a new mesh is formed that contains 35,219 vertices. The mesh refinement step requires only a few seconds on the C-90. The old solution is linearly interpolated onto the new mesh points and the flow solver is run for another 750 iterations with this as the starting solution.

The error indicator in Eq. (3), with K set from Fig. 2 to 17, is then used to both coarsen and refine the mesh. Once again, the surface shock and the acoustic wave receive the highest error values. Approximately 9000 vertices are removed from the mesh, and then 45,000 new vertices are added. Thus, the mesh points are redistributed in a way that better captures the HSI noise signal. The final mesh has 72,123 vertices, 389,949 tetrahedra, and 15,076 boundary faces. The flow solver is run for another 1000 iterations on this mesh, requiring about 85 CPU minutes.

Calculations for the $M_t = 0.90$ case proceeded in a similar manner. Comparable numbers of mesh points were targeted for coarsening and refinement at each adaption step. The final mesh contains 77,467 vertices, 421,030 tetrahedra, and 15,854 boundary faces. Figure 5 shows the mesh and the normalized pressure contours in the symmetry plane. Note that there are two levels of refinement at the shock, near the blade tip, and along the acoustic wave. The corresponding pressure contours show large gradients in these regions.

Mesh adaption for the $M_t = 0.88$ case proved to be more difficult. For the initial mesh, the curve-fit constant K is set from Fig. 3 to 92. Figure 3 also shows that the attenuation of the minimum pressure is not as linear as those for the higher-speed cases. This may be due to the fact that the acoustic wave for $M_t = 0.88$ is not delocalized. The straight-line curve-fits for the second and third meshes do not agree well with the data for $1.2 < r/R < 1.6$. It is expected that the error estimates will be underpredicted in this region, thereby reducing the probability of further refinement. However, both the blade surface and the far-field acoustic wave have correct error indicator values.

The first mesh refinement for the $M_t = 0.88$ case results in a grid that is similar in size to the $M_t = 0.95$ case. A large number of new grid points are added at the next coarsening/refinement step to test if the acoustic wave can be continuously targeted for a second level of refinement. This was unsuccessful, and most of the new points are placed near the far-field boundary. The final grid size is 121,383 vertices, 674,584 tetrahedra, and 20,510 boundary faces. Even with this large number of grid points, there is only one level of mesh refinement for the acoustic wave between $1.2 < r/R < 1.6$.

In retrospect, the same accuracy could have probably been obtained with far fewer grid points. This example demonstrates the importance of proper error scaling for the acoustic wave away from the blade tip. A more effective error indicator would have been to use a nonlinear error scaling function in Eq. (3) so as to better fit the pressure values in Fig. 3.

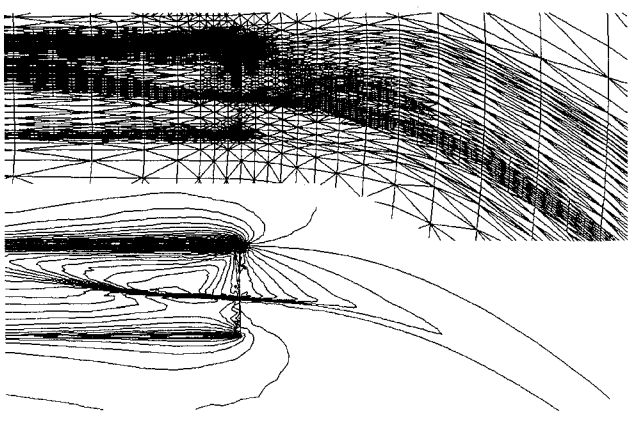

Fig. 5 Final mesh and computed pressure contours for $M_t = 0.90$.

Kirchhoff Formulation

Even though rotor HSI noise can be accurately computed with a CFD method, it is not practical to extend the computational domain beyond two or three rotor radii. The resulting large numbers of mesh points make this calculation prohibitive. An excellent solution to this problem, however, is to use a classical Kirchhoff integral formulation to compute the acoustic signals at arbitrary locations in the far field. As mentioned earlier, this type of approach has been used by a number of other researchers. The method presented here is similar to that used by Baeder et al.[11]; however, significant differences exist in the methods used to obtain the pressure derivatives on the Kirchhoff surface.

A classical Kirchhoff integral for a stationary surface can be written as

$$P(\boldsymbol{x}, t) = \frac{1}{4\pi} \int_S \left[\frac{\cos\theta}{r^2} P - \frac{1}{|\boldsymbol{r}|} P_n + \frac{\cos\theta}{a_\infty |\boldsymbol{r}|} P_t \right]_\tau \mathrm{d}S \quad (4)$$

The relevant terms in this equation can be described with reference to Fig. 6. Here, the observer is located at $\boldsymbol{x}$ with time t. The distance between the observer and a point on the Kirchhoff surface is given by $|\boldsymbol{r}|$, and θ is the angle between $\boldsymbol{r}$ and the normal $\boldsymbol{n}$ to the surface. P, P_n, and P_t are the acoustic pressure, and its normal and temporal derivatives, respectively, on the Kirchhoff surface. All pressure values and derivatives are evaluated at the time of emission τ, also referred to as the retarded time.

The speed of sound in Eq. (4) is given by a_∞, which is assumed to remain constant. This means that the cylindrical Kirchhoff surface must be placed at a radial distance that is sufficiently large so that flowfield nonlinearities are small. On the other hand, the CFD solution is less accurate as it gets farther away from the blade tip due to numerical dissipation. A good compromise location for the Kirchhoff surface was found to be at $r/R = 1.4$. The nonlinearities are small here, and the CFD solution is still highly accurate. This statement is backed up by computed results presented later in this article.

Two steps are required to evaluate the integral in Eq. (4). First, the Euler solution must be interpolated onto the Kirchhoff surface. The Kirchhoff surface is a two-dimensional Cartesian mesh with uniform spacing in the azimuthal direction and nonuniform spacing in the vertical direction. Contributions to the integral from the top and the bottom surfaces are neglected since the cylindrical surface extends out to about

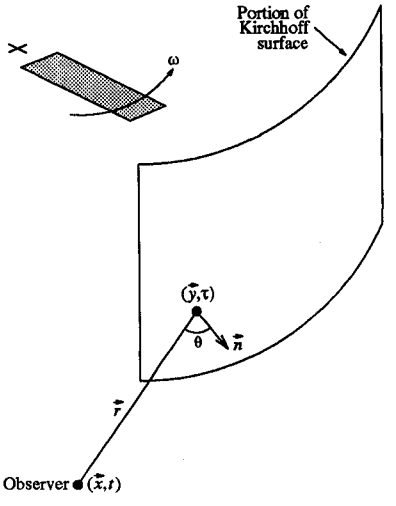

Fig. 6 Schematic for the Kirchhoff surface integration.

20 chord lengths above and below the plane of the rotor. Moreover, most of the HSI noise propagates in the rotor plane for the test cases in this article. The uniform azimuthal spacing is to facilitate the evaluation of the pressure field at the retarded time. It is important that this uniform mesh spacing be commensurate with the finest mesh spacing for the CFD grid. For the cases in this article, 7000 azimuthal mesh points are used, which more than exceeds this requirement. A total of 119 points are used in the vertical direction, with spacings similar to those in the CFD grid.

Pressure values for the Kirchhoff surface are linearly interpolated from the unstructured tetrahedral mesh. The two pressure derivatives are directly computed at the vertices by the flow solver and these are also interpolated onto the Kirchhoff mesh. It is important that the pressure derivatives be accurately evaluated in a manner that is consistent with the CFD solution algorithm. This means that these derivatives must be properly upwinded near impulsive flow features such as shocks.

The second step in solving the Kirchhoff integration in Eq. (4) is to evaluate the pressure terms at the retarded time τ. The delay between τ and the observer time t is the time it takes the acoustic signal to travel from the Kirchhoff surface to the observer:

$$t - \tau = |\boldsymbol{r}|/a_\infty \tag{5}$$

Because the rotor is in hover, the pressure values on the Kirchhoff surface at any retarded time can be determined by simply rotating the blade-fixed hovering solution around the azimuth. There is a one-to-one correspondence between time delay and azimuthal angle.

Comparisons with Experiment

Computed acoustic pressures from the three test cases can be compared to experimental results from Purcell.[6,7] He measured acoustic pressures from a $\frac{1}{7}$th scale model of a UH-1H rotor with two untwisted rectangular blades and NACA 0012 airfoil sections. These blades had a 3-in.-chord length and an AR of 13.71. A range of hover tip Mach numbers were tested from 0.85 to 0.95. Delocalization was found to occur between $M_t = 0.88$–0.90. For each Mach number, acoustic pressures were measured at four radial locations. The first location corresponded to the linear sonic cylinder ($r/R = 1/M_t$). The other three microphones were located at $r/R = 1.78$, 2.18, and 3.09. Results for $r/R = 2.18$ are very similar to those at $r/R = 1.78$ and are not reported here.

Figure 7 compares the computer predictions to experimental data for $M_t = 0.95$. The sonic cylinder result at $r/R = 1.053$ shows good agreement between computation and experiment for the general wave shape. The peak negative pressure is somewhat overpredicted, but the impulsive shock is well-captured by the computation. The acoustic wave is clearly delocalized, as evidenced by the asymmetry of the signal.

The $r/R = 1.78$ radial location shows computed results that have been obtained by three methods. The first result comes directly from the Euler solution on the final adapted mesh. The second is obtained by Kirchhoff integration on a surface

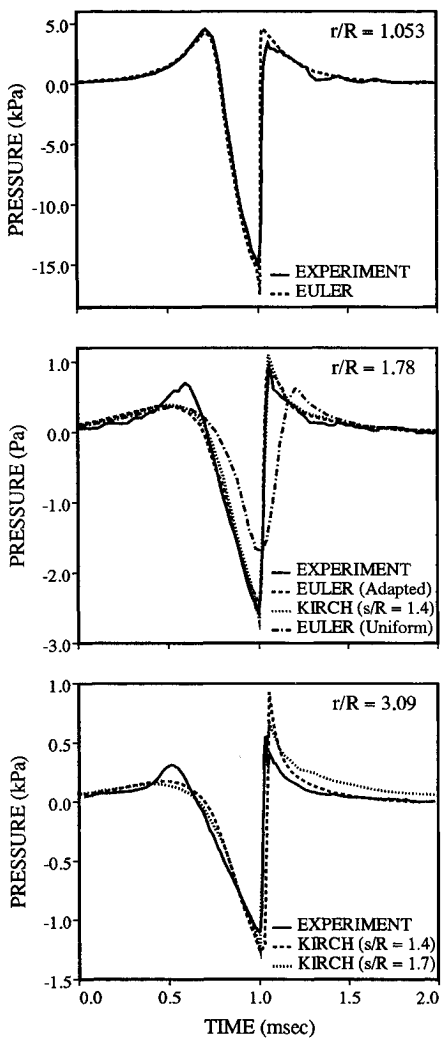

Fig. 7 Computed and experimental acoustic pressures for $M_t = 0.95$.

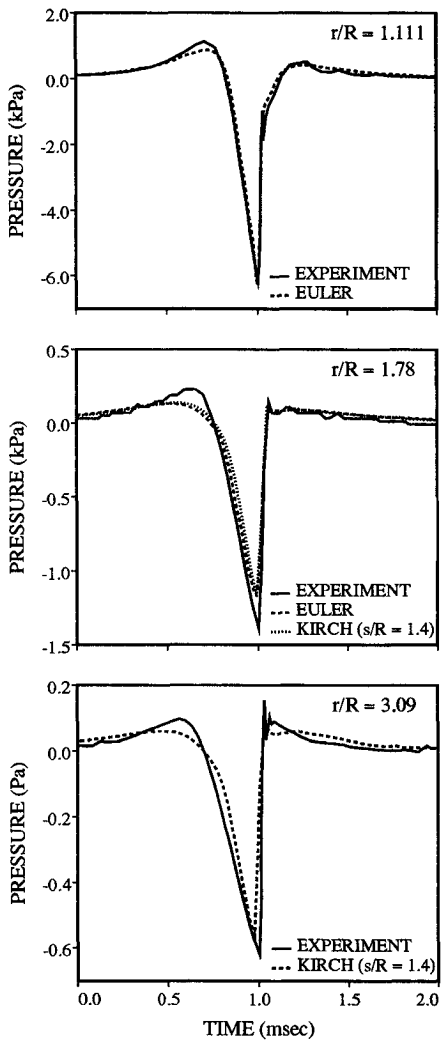

Fig. 8 Computed and experimental acoustic pressures for $M_t = 0.90$.

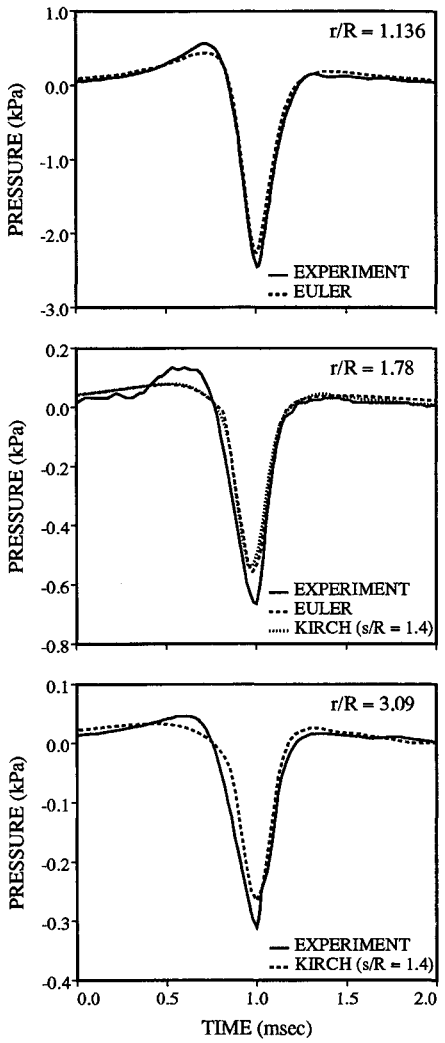

Fig. 9 Computed and experimental acoustic pressures for $M_t = 0.88$.

located at $s/R = 1.4$. The excellent agreement between the two computed results serves as a validation of the Kirchhoff approach as well as demonstrates the grid independence of the CFD solution near the outer boundary. Both solutions also show good agreement with experimental data except for a small region near the beginning of the acoustic signal. This discrepancy may be due to a lack of resolution of the CFD grid in this region. The error indicator in Eq. (3) targets edges for refinement that have large first derivatives. This strategy refines the mesh in the middle of the acoustic wave, but not so much at the beginning or the end. An error indicator that targets second derivatives of pressure might do a better job in these areas. The third computational result shows the solution on the initial coarse mesh and demonstrates the merits of the solution-adaptive method. This uniform-mesh solution excessively diffuses the impulsive signal, significantly underpredicts the minimum pressure, and severely distorts the general wave shape.

The acoustic pressure plots for $r/R = 3.09$ show similar good agreement with the data as was seen for the other two radial cases. The computed results are obtained by Kirchhoff integration on surfaces at two radial locations: $s/R = 1.4$ and 1.7. In general, the shape and duration of the acoustic signal is well-captured, but the magnitude of the peak negative pressure is slightly overpredicted. Results from these two integrations show excellent agreement with each other except for some small discrepancies at the end of the acoustic wave. The fact that the Kirchhoff results are insensitive to the surface location indicates that the effects of any nonlinearities beyond these Kirchhoff surfaces are small. It also provides evidence of grid independence of the Euler solution. If numerical dissipation were significant, then the far-field acoustic pressures would be affected by the location of the Kirchhoff surface.

Computed and experimental acoustic pressures for $M_t = 0.90$ are shown in Fig. 8. The sonic cylinder calculation at $r/R = 1.111$ shows excellent agreement with the data, both in the wave shape and the pressure magnitudes. However, the computed solutions at the other radial locations show that the peak negative pressure is slightly underpredicted. The general wave shapes are well-captured, including the impulsive noise and the pressure asymmetry.

Finally, Fig. 9 shows computed and experimental acoustic pressures for $M_t = 0.88$. This case is not delocalized, and the experimental and computational results show a more symmetrical wave shape than in the higher-speed cases. The comparison between experiment and computation is similar for all three radial locations. The general wave shape is well-captured, but the magnitude of the predicted peak negative pressure is approximately 10% too low at all radial locations. The excellent agreement between the Kirchhoff and Euler solutions at $r/R = 1.78$ shows that lack of grid resolution for either method is probably not the cause for this underprediction. Also, Baeder et al.[11] show very similar results for this case using their structured-grid Euler solver. Perhaps the inviscid approximation in the Euler solver has an effect on the computed results. The true flowfield around the blade tip involves localized flow separation and shock/boundary-layer interactions. The Euler solver does not model these, and their effect on the acoustic signals is not known.

Summary and Conclusions

In general, the computed results from all three cases show good agreement with Purcell's experimental data.[6,7] They also show excellent agreement with the structured-grid Euler calculations of Baeder et al.[11] The three cases span HSI noise conditions ranging from nondelocalized, to slightly delocalized, to fully delocalized. The overall adaptive-grid scheme works best for the two delocalized cases, which is not surprising, since these have the most clearly defined acoustic signals.

The results in this article represent the first time that solution-adaptive CFD methods have been used to model problems in helicopter acoustics. Although these capabilities were not specifically addressed in this article, the unstructured-grid approach provides greater flexibility in grid generation and mesh adaption around complicated rotor planforms, but requires more computational time than conventional structured-grid schemes.

The choice and scaling of an error indicator are crucial to the success of any adaptive-grid computation of HSI noise. The ability to locally refine the grid is only useful if new mesh points can be placed where they will improve the solution. In three dimensions, several thousand grid points can be easily wasted through the poor choice of an error indicator. We have developed a simple error indicator and a scaling factor that are appropriate for HSI noise. This article has demonstrated that the adaptive strategies that are used with this error indicator yield excellent results for HSI noise, particularly when the acoustic signals are strongly delocalized.

The combination of an Euler CFD method and a Kirchhoff formula is a powerful tool for the prediction of helicopter acoustics. The nonlinear three-dimensional and transonic effects near the blade tip are accurately modeled by the CFD solver and the Kirchhoff integral formula presents an efficient way to propagate these signals to the far field. Clearly, the next step is to implement these methods in forward flight.

Acknowledgments

R. Biswas' work was supported by NASA under Contract NAS 2-13721 with the Universities Space Research Association. The authors would like to thank J. D. Baeder for his

contributions during many discussions of this work, and also for his help with the initial grid generation.

References

[1]Schmitz, F. H., and Yu, Y. H., "Transonic Rotor Noise—Theoretical and Experimental Comparisons," *Vertica*, Vol. 5, No. 1, 1982, pp. 55–74.

[2]Ffowcs Williams, J. E., and Hawkings, D. L., "Sound Generation by Turbulence and Surfaces in Arbitrary Motion," *Philosophical Transactions of the Royal Society of London*, Vol. A264, No. 1151, 1969, pp. 321–342.

[3]Goldstein, M. E., *Aeroacoustics*, McGraw–Hill, New York, 1976, pp. 346–357.

[4]Purcell, T. W., Strawn, R. C., and Yu, Y. H., "Prediction of High-Speed Rotor Noise with a Kirchhoff Formula," AHS Specialists' Meeting on Aerodynamics and Aeroacoustics, Arlington, TX, Feb. 1987.

[5]Isom, M. P., Purcell, T. W., and Strawn, R. C., "Geometrical Acoustics and Transonic Helicopter Sound," AIAA Paper 87-2748, Oct. 1987.

[6]Purcell, T. W., "CFD and Transonic Helicopter Sound," 14th European Rotorcraft Forum, Paper No. 2, Milan, Italy, Sept. 1988.

[7]Purcell, T. W., "A Prediction of High-Speed Rotor Noise," AIAA Paper 89-1130, April 1989.

[8]Xue, Y., and Lyrintzis, A. S., "The Use of a Rotating Kirchhoff Formulation for 3-D Transonic BVI Far-Field Noise," AHS 49th Annual Forum, St. Louis, MO, May 1993.

[9]Baeder, J. D., "Euler Solutions to Nonlinear Acoustics of Non-Lifting Hovering Rotor Blades," 16th European Rotorcraft Forum, Paper II.3.3, Glasgow, Scotland, UK, Sept. 1990.

[10]Baeder, J. D., "Euler Solutions to Nonlinear Acoustics of Non-lifting Rotor Blades," International Technical Specialists Meeting on Rotorcraft and Rotor Fluid Dynamics, Philadelphia, PA, Oct. 1991.

[11]Baeder, J. D., Gallman, J. M., and Yu, Y. H., "A Computational Study of the Aeroacoustics of Rotors in Hover," AHS 49th Annual Forum, St. Louis, MO, May 1993.

[12]Barth, T. J., "A 3-D Upwind Euler Solver for Unstructured Meshes," AIAA Paper 91-1548, June 1991.

[13]Strawn, R. C., and Barth, T. J., "A Finite-Volume Euler Solver for Computing Rotary-Wing Aerodynamics on Unstructured Meshes," *AHS Journal*, Vol. 38, No. 2, 1993, pp. 61–67.

[14]Biswas, R., and Strawn, R. C., "A New Procedure for Dynamic Adaption of Three-Dimensional Unstructured Grids," *Applied Numerical Mathematics*, Vol. 13, No. 6, 1994, pp. 437–452.